



A Comparison of Image-Based and Physics-Based Atmospheric Correction Methods for Extracting Snow and Vegetation Cover in Nepal Himalayas Using Landsat 8 OLI Images

K. C. Niraj¹ · Sharad Kumar Gupta² · Dericks Praise Shukla¹

Received: 21 January 2021 / Accepted: 23 September 2022 / Published online: 21 October 2022
© Indian Society of Remote Sensing 2022

Abstract

Applying atmospheric corrections on satellite images is an important step before using the satellite image for any further processing. These atmospheric corrections are broadly classified as either image-based or physics-based atmospheric corrections. From a plethora of such corrections, which is best suited for vegetation and snow mapping in the mountainous Himalayan region needs to be decided. Hence, in this work, we evaluated a total of eight atmospheric corrections models including 5 image-based namely DOS (dark object subtraction method), improved dark object subtraction method (DOS3), COST (cosine theta), apparent reflectance (Aref), QUAC (QUick Atmospheric Correction), and 3 physics-based methods, namely SIAC (Sensor Invariant Atmospheric Correction), 6SV (Second Simulation of the Satellite Signal in the Solar Spectrum) and FLAASH (Fast Line-of-sight Atmospheric Analysis of Spectral Hypercubes). We found that 6SV and FLAASH were better than other methods and QUAC was the worst performer when applied to Landsat 8 OLI images of the Nepal Himalayan region which has dense vegetation and snow-covered areas. The better snow reflectance values were observed for FLAASH (B, G, R: 0.88, 0.89, 0.9; NIR: 0.83), SIAC (B, G, R: 0.85, 0.89, 0.89; NIR: 0.83) and 6SV (B, G, R: 0.87, 0.89, 0.89; NIR: 0.8) methods, whereas the FLAASH and SIAC methods exhibited higher vegetation reflectance values in the NIR band than other methods. The spectra from the standard spectral library were compared with the values of vegetation and snow spectral reflectance produced from corrected reflectance images. The mean values of snow and vegetation reflectance were higher for FLAASH, 6SV, and SIAC methods as compared to other methods. Therefore, FLAASH, 6SV, and SIAC methods, in contrast to other used atmospheric correction methods, have a high possibility of giving accurate snow and vegetation cover mapping. The snow cover and vegetation cover map prepared using NDSI and NDVI showed that areas covered under thin clouds and haze were better extracted when FLAASH, SIAC, and 6SV methods are applied as compared to other methods. Thus, this study confirms that physics-based atmospheric correction models such as FLAASH, SIAC, and 6SV methods should be used while working on satellite images of the Himalayan region where the focus is on snow and vegetation cover mapping.

Keywords Image-based atmospheric correction · Physics-based atmospheric correction · SIAC · 6SV · FLAASH · Himalayan region

✉ Dericks Praise Shukla
dericks@iitmandi.ac.in

K. C. Niraj
d18058@students.iitmandi.ac.in

Sharad Kumar Gupta
sharadgupta@tauex.tau.ac.il

¹ School of Civil and Environmental Engineering, Indian Institute of Technology-Mandi, Mandi, Himachal Pradesh, India

² School of Environment and Earth Sciences, Faculty of Exact Sciences, Tel Aviv University, 6997820 Tel Aviv, Israel

Introduction

The multispectral satellite image from Landsat 8 OLI and the thermal infrared sensor (TIRS) recorded continuous information about the earth's surface as digital numbers (DN). These DN values are maintained in a wide range of electromagnetic spectrum ranges, from the lowest wavelength Band-1 coastal aerosol (0.43–0.45 μm) to the highest wavelength Band-11 Thermal infrared TIRS2 (11.50–12.51 μm), with 16-bit radiometric resolution.

Before using Landsat 8 OLI data for various applications, such as mapping land resources (snow, vegetation, water, etc.) and others, satellite images must first be radiometrically, atmospherically, and geometrically adjusted. Since Landsat 8 OLI data have already been geometrically adjusted, comparing and analyzing images taken throughout several seasons is easy.

In order to eliminate scattering and absorption effects caused by the atmosphere’s particles and gases, radiometric and atmospheric correction is mostly applied to satellite images. The incoming radiation from the source (the sun) travels a long distance to interact with targets on the earth’s surface, traveling through the atmosphere (Fig. 1). E_0 (solar illumination at the top of the atmosphere) interacts with various particles, gases, and molecules in the upper atmosphere once it has radiated from the source (Thorne et al., 1997; Paolini et al., 2006; Jensen, 2009). As a result of absorption and scattering, energy is attenuated (Liou, 2002). The quantity of energy that reaches the earth’s surface is determined by T_Θ (atmospheric transmittance), where Θ is the zenith angle (Sabins, 1987). When incoming radiation (irradiance) interacts with surface features, it bounces back as R_H (house reflectance), R_R (rock stratum reflectance), and R_V (vegetation reflectance) as shown in Fig. 1. Radiation (energy emitted from the earth’s surface) from diverse characteristics conveys information about the subject of interest (Jensen, 2009). E_{sun} (diffuse sky irradiance) or radiation from nearby places on the

ground are both included in the surface reflectance (Sabins, 1987).

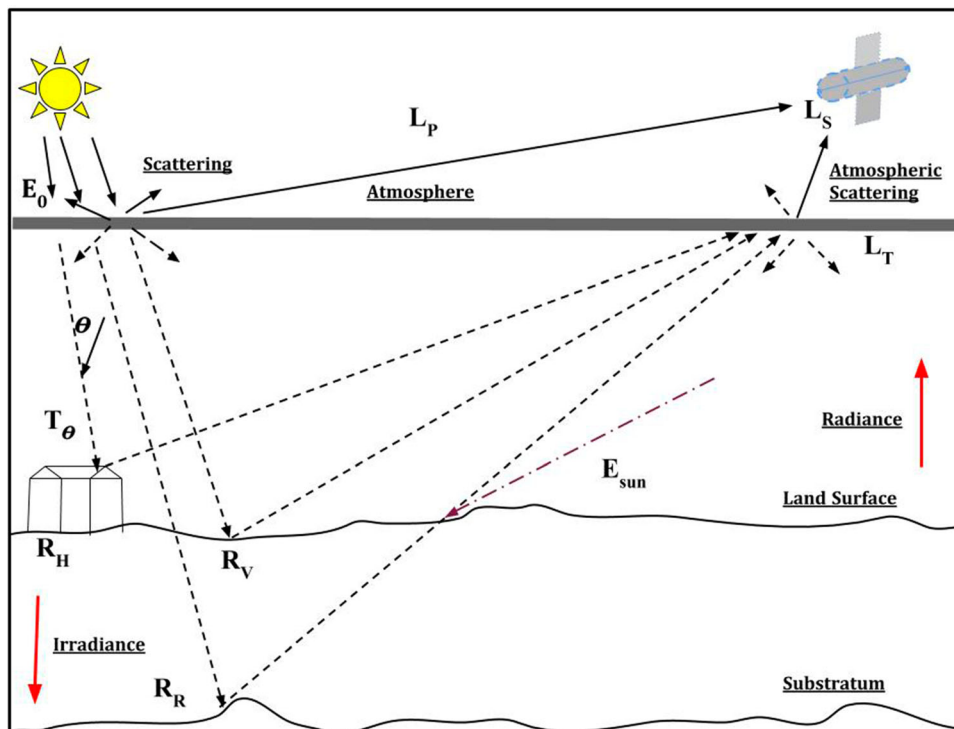
The path radiance (L_p) and E_{sun} in remote sensing data often provide unwanted radiometric and atmospheric distortions, complicating image interpretation for a variety of applications. Irradiance is radiated toward the sensor after bouncing back off the earth’s surface (Paolini et al., 2006). This path is again subjected to scattering and absorption effects due to interaction within the atmosphere (Slater, 1985). Finally, the total amount of energy recorded by the sensor is explained by the equation (Jensen, 2009):

$$L_s = L_T * T_\theta * R_T * H + L_p \tag{1}$$

where L_s = total energy recorded at the sensor, R_T = total reflectance from the earth targets, H = total irradiance.

The recorded DN values at the sensor are a function of sun-sensor geometry, sun elevation, atmosphere (scattering, absorption), topography, and surface model. Atmospheric correction is crucial for land resource mapping applications where ground reflectance is more significant than at sensor reflection (Slater, 1985). Through scattering, absorption, and refraction, the atmosphere distorts the radiance recorded by the satellite sensor (Chavez, 1996). Two well-known scatterings, i.e., Rayleigh and Mie scattering, characterize realistic atmospheric scattering relationships (Chavez, 1996). According to Rayleigh scattering, relative scattering is inversely proportional to the fourth power of wavelength ($\lambda^{-4} = 1/\lambda^4$), implying that shorter wavelengths of the electromagnetic spectrum

Fig. 1 The simplified schematic diagram of the atmospheric interference and the passage of electromagnetic radiation from the Sun to the land surface and then to the satellite sensor



scatter more than longer wavelengths (Chavez, 1989) Blue and green, for example, scatter more than the red and NIR bands. This type of scattering is mainly produced by gas molecules that are much smaller than the incoming wavelength (Chavez, 1996). According to the Mie scattering phenomenon, the scattering is inversely proportional to wavelength and is normally for a medium atmosphere, i.e., ($\lambda^{-1} = 1/\lambda$) (Chavez, 1989). Though this relationship can vary from λ^0 to λ^{-4} , where λ^0 represents complete scattering, i.e., cloud cover (Hall et al., 1991). Mie scattering is caused by coarser size particles that are around the same size as the wavelength such as smoke and dust.

There are several ways of atmospheric correction that can be used to restrict the effects of scattering and absorption on the atmosphere (Moran et al., 1992). One way is focused on image-based correction methods, which are divided into two categories: absolute and relative atmospheric adjustments (Yuan & Elvidge, 1996). Relative standardization methods are a way of comparing each image's spectral properties to a reference image such that each altered image seems to have been captured with the same sensor and under similar atmospheric conditions as the reference image (Yuan & Elvidge, 1996). For modifying atmospheric effects based on a complete image or permanent portions, there are several processes available for relative normalization methods such as QUAC (Quick Atmospheric Correction). The relative normalization image-based atmospheric correction model is based on the original satellite image's unique DN values and does not require any atmospheric information (Baisantry et al., 2012). The overall concept of relative normalization assumes that different glances on comparable items from different dated focuses or multiple bands should compensate for atmospheric effects (Barnas et al., 2019). In any case, the atmospheric pathways from several looks must be identical, which is impossible to achieve. On the other hand, the absolute atmospheric correction approaches rely on a thorough understanding of atmospheric factors to change each image individually (Lu et al., 2002). Rather than reverting to a reference image, it uses data from a portion of the image. The haziest zones, for example, are removed and applied to the rest of the image. Estimated parameters were substituted for the extracted data (Caselles et al., 1989). Absolute or physically based calibration approaches, which rely on atmospheric information (Richards, 1993), are considered to be more precise. Dark object subtraction (DOS), improved dark object subtraction (DOS3), cosine theta (COST), and apparent reflectance techniques were included in the absolute image-based correction model (Chavez, 1989). Histogram altering of single-date imagery and multi-date imagery standardization based on histogram coordinating or regression modeling was among the models used. The absolute image-

based atmospheric correction method produces more favorable outcomes than relative standardization strategies (Cui et al., 2014). Physics-based correction techniques involving the radiative transfer models are another means of adjusting the impacts of atmospheric scattering and absorption on satellite images (Wang et al., 2019). For the purpose of removing the effects of scattering and absorption, three well-known physics-based atmospheric correction algorithms are FLAASH (Fast Line-of-Sight Atmospheric Analysis of Spectral Hypercubes), 6SV (a modified version of Second Simulation of the Satellite Signal in the Solar Spectrum), and SIAC (Sensor Invariant Atmospheric Correction) (Yin et al., 2019; Wang et al., 2019), while QUAC is predicated based upon dark object assumption, FLAASH and 6SV are based on radiative transfer models (Wang et al., 2019). In contrast, SIAC is based on a data fusion technique that first tries to incorporate uncertainty data from several data sources before carrying out the atmospheric correction of satellite images (Yin et al., 2019). The FLAASH and ATCOR atmospheric correction technologies allow for greater accuracy (Matthew et al., 2002). However, this module is licensed and so cannot be used without authorization. As a result of its excellent accuracy and online availability at <http://6s.ltdri.org>, the 6SV model is frequently utilized today to reduce atmospheric distortions (Kim et al., 2022). In addition, it is possible to develop the 6SV model particularly to identify the right parameters that will yield the highest level of accuracy (Kim et al., 2022). Aerosols, water vapor, and ozone are examples of atmospheric characteristics that influence the accuracy of the results of atmospheric correction in FLAASH, ATCOR, and 6SV, but, field measurements of these parameters are rarely available. This can be addressed by using satellite data, particularly MODIS Terra/Aqua data, which is available very instantly (Chen et al., 2010; Basith et al., 2019).

The results of both physics-based and image-based atmospheric correction techniques primarily reduce atmospheric (absorption and scattering) effects, and they can be successfully used for mapping land resources (vegetation, snow, etc.) (Paul, 2000; Huete et al., 1999). Early snow climatology researchers mapped the locations of snow cover using a variety of ground-based and airborne photographic survey techniques (Bhambri et al., 2011). In difficult and remote river basins, the ground-based monitoring strategy is exceedingly labor-intensive, costly, and even dangerous (Kaushik et al., 2019). As a result, field surveys are unsuitable for mapping rapidly melting snow cover in difficult terrain. Aerial and satellite surveys, as opposed to field surveys, are the easy method that offers more comprehensive information in a shorter amount of time (Barnas et al., 2019; Kaushik et al., 2019). In response to natural disasters like ice avalanches, landslides, forest

fires, etc., changes in the creation and distribution of snow and vegetation extent may stand out. Ice avalanches could result in mud/debris flows, dammed rivers, or glacial lake outburst floods (GLOFs) (Navalgund et al., 2007). It is necessary to identify and map the snow zones that are prone to these risks through ongoing snow location monitoring (using NDSI data). When determining snow cover and melting in conjunction with other factors including weather, soil type, and hydrology, snow indices (mainly Normalized Difference Snow Index–NDSI) have been widely used in climate change research (Crippen, 1988; Paul, 2000; Andreassen et al., 2008; Selkowitz & Forster, 2016). A loss of biodiversity and the extinction of innumerable plant and animal species are both potential consequences of climate change (Phillips, 1997). For mapping and monitoring the extent of vegetation loss due to changing climate and land use patterns, vegetation indices (mainly Normalized Difference Vegetation Index–NDVI) are very useful (Domenikiotis et al., 2003). Changing lighting conditions, surface slope, and viewing angle must be taken into account while using NDVI (Matsushita et al., 2007). Thus, NDVI is sensitive to the color of the underlying soil and does have a propensity to get saturated over dense vegetation (Domenikiotis et al., 2003; Matsushita et al., 2007).

The objective of this study involves applying and comparing image-based atmospheric correction as well as physics-based atmospheric correction techniques on Landsat 8 OLI images. The spectral reflectance of vegetation and the snow cover areas are taken from each atmospherically corrected image and compared to the spectral libraries provided by the ENVI software. We also investigated the effects of NDSI and NDVI from various correction techniques for mapping snow cover and vegetation cover maps. For each reflectance image, the NDSI and NDVI are calculated, which can be further classified based on distinct snow and vegetation threshold values.

Materials and Methods

Study Area

This study was carried out in the Manang, Mustang, Kaski, Lamjung, and Myagdi districts of Gandaki province Nepal as shown in Fig. 2. Manang, Mustang, Kaski, Lamjung, and Myagdi districts having the spatial extent between latitude 28° 54' 2.06'' N to 28° 26' 42.51'' N and longitude from 83° 47' 20.86'' E to 84° 34' 13.5'' E, 29° 19' 53.32'' N to 28° 33' 53.45'' N and longitude from 83° 28' 46.29'' E to 84° 15' 7.96'' E, 28° 36' 48.81'' N to 28° 4' 40.31'' N and

longitude from 83° 42' 1.74'' E to 84° 16' 42.83'' E, 28° 30' 37.4'' to 28° 3' 20.51'' N and longitude from 84° 11' 12.01'' E to 84° 41' 40.9'' E and 28° 47' 37.98'' to 28° 17' 53.86'' N and longitude from 83° 5' 59.31'' E to 83° 52' 17.22'' E, respectively. Manang, Mustang, Kaski, Lamjung, and Myagdi districts of Nepal which are located in the Dhawalagiri Zone and part of Gandaki province lies in Northern Nepal. The elevation of the Manang and Mustang district ranges from 1000 to 2000 m in the subtropical climate to 3000–6400 m in the Trans-Himalayan climate zone (Pant et al., 2018; Basnet et al., 2019). The elevation of the Kaski, Myagdi, and Lamjung districts ranges from 300 to 1000 m in the upper tropical climate zone to 3000–6400 m in the Trans-Himalayan climate zone. The important rivers of the provinces are Kaligandaki, Budhigandaki, Marsyangdi, Modi, Madi, Daraudi, Seti, Aandhikhola, Badigad, and Uttarganga. The top half of the Manang, Mustang, and Kaski districts encompass the country's high mountainous range, which feeds thousands of glacial lakes, many of which are vulnerable to glacial lake outburst floods (GLOFs) due to rapid glacial retreat (Pant et al., 2018; Basnet et al., 2019). Tilicho glacial lake, Thulagi glacial lake, and Karpuche glacial lake are the most well-known glacial lakes in Nepal (Pant et al., 2018; Basnet et al., 2019). There are other glacier lakes in Gandaki province. Aside from glacier lakes, Gandaki province has a lot of semi-natural freshwaters (stream-fed) lakes. Fewa, Begnas, and Rupa Lakes are some of the most well-known semi-natural freshwater lakes in the Kaski district. The administrative boundary of Nepal is depicted in Fig. 1a, and the location of the research area is shown in Fig. 1b, c. The original DN Landsat 8 OLI histogram equalized false-color composite (FCC) image is displayed in Fig. 1c. As seen in Fig. 1c, Myagdi, Kaski, and Lamjung districts have extensive vegetation available at lower elevations, but Manang and Mustang districts have a lot of snow cover, rocky terrain, and little vegetation cover.

Data and Software Used

Landsat 8 OLI satellite images, was downloaded from the USGS image database site (<http://earthexplorer.usgs.gov>) and used in this study. Landsat 8 OLI is the primary data source for this study, as seen in Table 1. By selecting and averaging end-member spectra from a large number of natural and artificial library reflectance spectra, the “universal” reference spectrum is created. An example library from the spectral libraries offered with ENVI was used as the reference in this work. Python 2.7, Arc map 10.6, ENVI 5.3, and other applications were utilized to carry out this work.

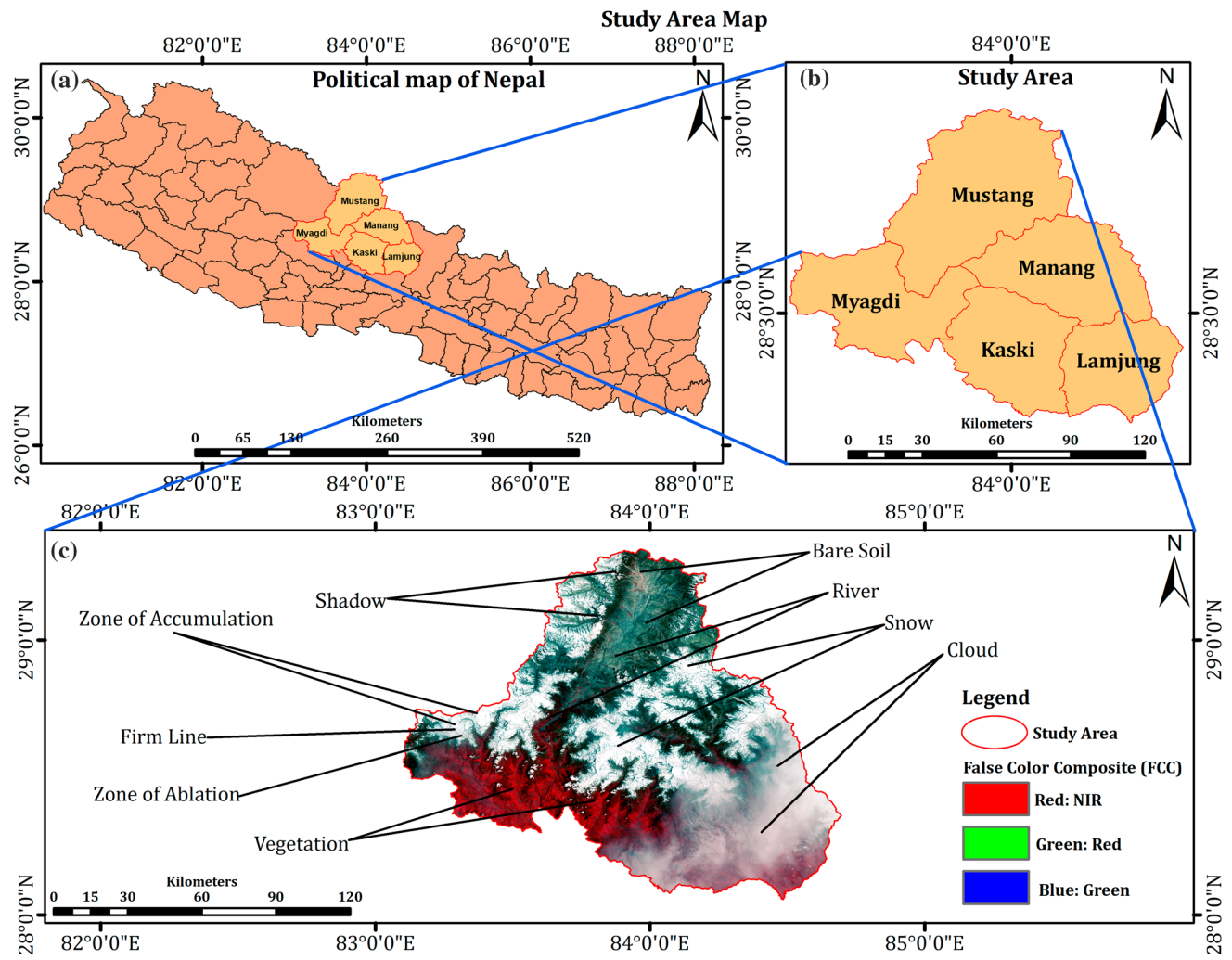


Fig. 2 The study area map showing the location of 5 sub districts on the false-color composite (FCC) image using NIR, Red, and Green bands of Landsat 8 OLI satellite data. Dense vegetation is shown in reddish tone, snow covered areas in whitish tone and clouds/ haze in the eastern portion of the study area

Table 1 The information about the Landsat 8 OLI datasets utilized in this study are shown here

Landsat 8	Bands	Wavelength micrometers	Resolution (meters)	Date of acquisition mm/dd/yy
Operational Land Imager (OLI)	Band 2-Blue	0.45–0.51	30	5/20/2020
	Band 3-Green	0.53–0.59	30	
	Band 4-Red	0.64–0.67	30	
	Band 5-Near-Infrared (NIR)	0.85–0.88	30	
	Band 6-Shortwave Infrared (SWIR) 1	1.57–1.65	30	
	Band 7-Shortwave Infrared (SWIR) 2	2.11–2.29	30	

Methodology

Radiometric Calibration

Digital numbers (DN) refer to the perfectly reflected radiance above the earth's atmosphere as well as the recorded signals reaching the sensor from various targets on the ground surface (Chavez, 1989; Hall et al., 1991). Digital numbers ranging from 0 to 65,535 are assigned to Landsat 8 images (Schroeder et al., 2006). Radiometric calibration is a method of directly converting DN measurements to radiance, and it necessitates knowledge of the sensor's gain and bias in each band (Paolini et al., 2006). The sensor is radiometrically calibrated before it is launched, however the sensor position changes with time, resulting in erroneous images (Lu et al., 2002). The sensor should be recalibrated regularly to avoid this issue. In general, there are two processes in radiometric calibration for DN values (Asra, 1989): First, use the gain and bias information for each Landsat 8 band in Appendix 2 to convert DN values to spectral radiance at the sensor. The following equation (Price, 1987; Chavez, 1996) can be used to convert the satellite Digital number (DN) to radiance at the satellite:

$$L_{\text{sat}} = [G * \text{DN}] + B \quad (2)$$

where L_{sat} = at sensor spectral radiance ($\text{W m}^{-2} \text{sr}^{-1} \mu\text{m}^{-1}$); DN = the digital number for the given spectral band; G = slope of the calibration function (channel gain); B = intercept of the calibration function.

Appendix 2 shows the Gain and Bias values used for Landsat 8 OLI spectral bands, and they are not repeated here. The conversion to TOA (top of atmosphere) reflectance with sun angle adjustment is the next stage. For Landsat 8 data, the following equation is used to convert DN values to TOA reflectance: (Chavez, 1989; Hall et al., 1991)

$$\rho\lambda' = \frac{((G * \text{DN}) + B)}{\cos(\theta_{\text{sz}})} \quad (3)$$

where $\rho\lambda'$ = TOA planetary reflectance, with solar angle correction; θ_{SZ} = Local solar zenith angle; $\theta_{\text{SZ}} = 90$ -sun elevation.

Apparent Reflectance (A_{ref}) Method

The apparent reflectance method transforms radiance into reflectance at the sensor in a simple manner (Cui et al., 2014). The satellite sensor, it's known as the TOA/planetary reflectance (Cui et al., 2014; Gupta & Shukla, 2020). Although this method improves solar irradiance and solar

zenithal angle, it does not account for atmospheric scattering and absorption (López-Serrano et al., 2016). After determining the E_{sun} , the apparent reflectance at the satellite sensor is calculated using the following equation (Chavez, 1996; Gupta & Shukla, 2020):

$$A_{\text{ref}} = \frac{(\pi * d^2 * L_{\text{sat}})}{E_{\text{sun}} * \cos(\theta_{\text{sz}})} \quad (4)$$

where d = Earth–Sun distance in astronomical units; E_{sun} = Mean solar exoatmospheric irradiance.

Above Eq. (4) can be written as:
 $A_{\text{ref}} = \text{Radiance}/\text{Irradiance}$

Radiance is the amount of energy emitted by the earth. Radiance is the total quantity of energy measured by the sensor. Irradiance is the amount of sunlight that reaches the Earth and interacts with the land surface and sub-surface characteristics. The apparent reflectance measured at the sensor for a satellite image is also known as unit less TOA planetary reflectance at the satellite, which has values ranging from 0 to 1. (0% to 100%). Only the E_{sun} value is needed for atmospheric corrections to obtain the correct reflectance of Earth features which was determined using the above standard equation of TOA planetary reflectance ($\rho\lambda'$).

Atmospheric Correction

Atmospheric corrections are the process of removing or limiting atmospheric effects (scattering, absorption, and refraction) that appear in the entire image when the sensor records surface radiance due to atmospheric attenuation (Chavez, 1996; Paolini et al., 2006). Absolute and relative atmospheric correction procedures are the two most common forms of image-based atmospheric correction (Song et al., 2001). Adjusting the effects of scattering and absorption to attain true ground surface reflectance is known as an image-based atmospheric correction (Thorne et al., 1997). In this study, image-based correction techniques and physics-based correction methods are used to correct the distortions. The image-based atmospheric correction techniques that are used in this paper, are Dark Object Subtraction (DOS), Improved Dark Object Subtraction (DOS3), and COST (cosine theta) and QUAC approaches, while the physics-based atmospheric correction techniques used in this work include FLAASH, SIAC, and 6SV.

The conventional atmospheric correction equation, which may be used with any image-based correction technique, is as follows: (Chavez, 1989; Chavez, 1996):

$$\rho_{Tref} = \frac{\pi * d^2 * (L_{sat} - L_{Haze})}{T_v * (E_{sun} * \cos \theta_{SZ} * T_z) + E_{down}} \tag{5}$$

where ρ_{Tref} = correct spectral reflectance of the surface (takes value 0–1); L_{Haze} = path radiance (upwelling atmospheric spectral radiance) scattered in the direction of and at the sensor ($W\ m^{-2}\ sr^{-1}\ km^{-1}$); T_v = atmospheric transmittance along the path from the ground surface to the sensor; E_{sun} , is mean solar exoatmospheric irradiance; T_z = atmospheric transmittance along the path from the sun to the ground surface; E_{down} = downwelling spectral irradiance at the surface ($W\ m^{-2}\ \mu m^{-1}$).

The method provided in this study uses the same assumption as (Schroeder et al., 2006), but applies it to Landsat 8 satellite data for glacial applications. Table 2 lists the necessary values for T_z , T_v , L_{Haze} , and E_{down} .

Haze Estimation

The process of adjusting path radiance (L_p) and upwelling atmospheric scattering induced by scattering and absorption is known as haze estimation (Richter, 1996). Selecting SHV (Starting haze value) was the most accurate way of evaluating haze. For the visible, NIR, SWIR1, and SWIR2 bands, this study calculates the DN pixel value of the dark object (SHV). L_1 percent (0.01) denotes the fraction of pixels that have been determined to be SHV (Richter, 1996). The histogram is displayed with its finest SHV after defining the dark pixel proportion, as illustrated in Fig. 3. Because maximal scattering occurs in band 1, SHV (DN values) are highest in band 1 (blue) and lowest in band 4 (NIR) in Fig. 3. The DOS method employs the atmospheric haze decay model, which states that scattering is greatest in the blue wavelength, reduces in the NIR, and then increases in the SWIR1 and SWIR2 bands.

Dark Object Subtraction Method (DOS)

The dark object subtraction method (DOS) is likely the most straightforward and consistent procedure among the majority of widely used image-based atmospheric correction procedures (Song et al. 2001). This technique implies

Table 2 The values of the parameters used in four different image-based atmospheric correction methods

Method	T_z	T_v	E_{down}	L_{haze}
Apparent Reflectance	1	1	0	0
DOS	1	1	0	SHV
COST	$\cos(\theta_{sz})$	$\cos(\theta_v)$	0	SHV
DOS3	Iterative	Iterative	Iterative	Iterative

the presence of dark objects that correspond to the Landsat 8 band’s minimum DN value (Q_{Min}). The minimal dark object DN value (Q_{Min}) is chosen based on statistical data for each band. The histogram is used to calculate the (Q_{Min}) value for each Landsat 8 OLI band. Typically, the DOS approach scans each band for the darkest pixel value, then subtracts this value from every pixel in the distinct Landsat 8 OLI band to reduce the scattering impact in the scene (Song et al., 2001). The Dark Object Subtraction (DOS) approach removes the haze component from remote sensing data caused by additive scattering (Chavez, 1989). The DOS correction is based on the assumption that the maximum number of true black pixels in satellite images contains 1% of actual ground reflectance. The following equation (Chavez, 1989) was used to determine the amount of haze effects in the satellite image used in this study:

$$L_{1\%} = 0.01 * \frac{E_{sun} * \cos \theta_z}{\pi * d^2} \tag{6}$$

$$L_{Haze} = SHV_{rad} - L_{1\%} \tag{7}$$

where SHV_{rad} = starting haze value which values alike to minimum DN (digital numbers) value of the scene.

The calculated haze value and other required parameter values are applied in the above standard equation of atmospheric correction to obtain true ground reflectance. A new SHV value must be computed for each band.

Improved DOS Method (DOS3)

The improved DOS method uses information from a single band to calculate L_{Haze} values for the remaining bands of an image using atmospheric scattering functions. Because scattering is band dependent, i.e., visible bands (Blue, Green, and Red) with shorter wavelengths are more affected by atmospheric scattering function as compared to longer wavelength bands (NIR and SWIR). The improved DOS method denoted DOS3 uses the standard DOS methodology in computation, except for the atmospheric transmittance (T_v) (Paolini et al., 2006; Song et al., 2001). The T_v value was calculated as:

$$T_v = \exp\left(\frac{T_{AUR}}{\cos \theta_{SZ}}\right) \tag{8}$$

where T_v = atmospheric transmittance along the path from the sun to the ground surface; T_{AUR} = optical thickness of Rayleigh scattering which is calculated according to Kaufman (1989).

$$T_{AUR} = 0.008569 * \lambda^{-4} * (1 + 0.0113 * \lambda^{-2} + 0.00013 * \lambda^{-4}) \tag{9}$$

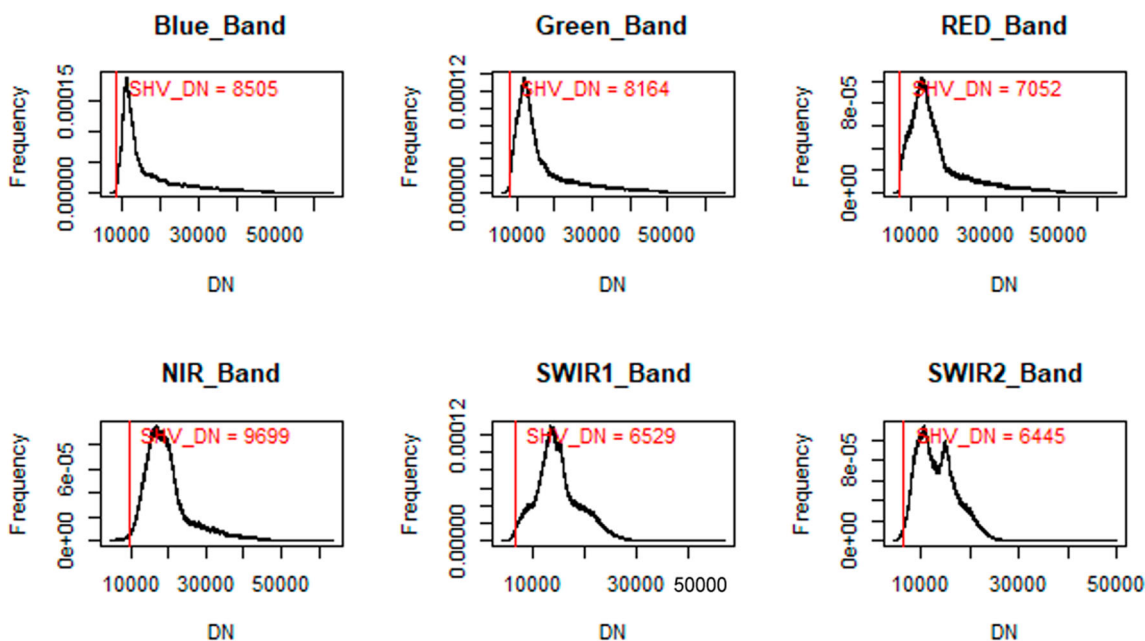


Fig. 3 The graph shows the starting haze value (SHV) for each band of Landsat 8 OLI

Table 3 The value of the specific scattering function for Landsat 8 OLI bands that are used in this study. The values in parenthesis are in percentage

Bands	Central wavelength (λ)	Scattering Function				
		Rayleigh Very clear λ^{-4} (%)	Mie Clear λ^{-2} (%)	Mie Moderate λ^{-1} (%)	Mie Hazy $\lambda^{-0.7}$ (%)	Mie Completely Mie $\lambda^{-0.5}$ (%)
Band 2-Green	0.48	18.84 (51.73)	4.34 (36.97)	2.08 (27.37)	1.67 (24.20)	1.44 (21.98)
Band 3-green	0.56	10.17 (27.93)	3.19 (27.17)	1.79 (23.55)	1.5 (21.74)	1.34 (20.46)
Band 4-Red	0.66	5.43 (14.91)	2.3 (19.59)	1.52 (20.00)	1.34 (19.42)	1.23 (18.78)
Band 5-Near-infrared (NIR)	0.87	1.79 (4.34)	1.32 (11.24)	1.15 (15.13)	1.1 (15.94)	1.07 (16.34)
Band 6-Shortwave infrared (SWIR) 1	1.61	0.15 (0.41)	0.39 (3.32)	0.62 (8.16)	0.72 (10.43)	0.79 (12.06)
Band 7- Shortwave infrared (SWIR) 2	2.20	0.04 (0.11)	0.21 (1.79)	0.45 (5.29)	0.58 (8.41)	0.67 (10.23)
Total		36.42	11.74	7.60	6.90	6.55

where λ is the central wavelength of each band, in microns. The value for the atmosphere scattering function for individual Landsat 8 bands is given in Table 3.

COST (cosine theta) Method

The COST atmospheric correction method was the first to report on the multiplicative effects of atmospheric

scattering and absorption. This means that the COST approach is a modification of the DOS model that includes the $\cos(\Theta_{sz})$ term. The COST model is primarily used to correct atmospheric transmittance along the path from the sun to the ground surface (T_z), which is multiplicative but not additive. For the COST method:

- $T_z = \cos(\Theta_{sz}) = \cos$ (solar zenithal angle)

- $T_V = \text{Cos}(\Theta_{sv}) = 1.0$ because Θ_{sv} is zero degrees for nadir view.

QUAC (QUick Atmospheric Correction) Method

The image-based atmospheric correction method, QUAC, simply needs a rough description of the sensor band positions (i.e., center wavelengths) and their radiometric calibration; no extra metadata is needed (Prosperi, 2012). Compared to physics-based approaches, QUAC is significantly faster but also more approximate because it does not employ first principles radiative transfer calculations (Bernstein et al., 2012) rather it uses dark targets (Wang et al., 2019). Three hypotheses are taken into account: (1) the image must contain more than 10 spectrally distinct pixels; (2) the standard deviation of the reflectance from end-member pixels is spectrally independent and can be used to calculate the transmittance; and (3) there is a sufficient number of dark pixels to calculate an invariant baseline, assumed as a measurement of attenuation (scattering and absorption) and the adjacency effect (Bernstein et al., 2005).

SIAC (Sensor Invariant Atmospheric Correction) Method

A coarse resolution simulation of the earth's surface is used in SIAC using the MODIS MCD43 BRDF (Bidirectional Reflectance Distribution Function) product. To deal with the scale discrepancies between MODIS and Landsat 8 OLI, a model based on MODIS PSF is applied (Yin et al., 2019). In order to solve for the atmospheric parameters, we couple the ECMWF CAMS prediction with the 6SV model and utilize it as a prior for the atmospheric states. The atmospheric parameters are obtained from high temporal resolution MODIS observations to get the BRDF description of the earth's surface, and the atmospheric state is provided by the ECMWF CAMS near-real-time data (Yin et al., 2019). This work was carried out in Python 2.7 having integration in Google colab and Google Earth Engine.

6SV (Second Simulation of the Satellite Signal in the Solar Spectrum) Method

This physics-based atmospheric correction method makes predictions about objects' reflectance (A_{ref}) at the top of the atmosphere (TOA) based on data about surface reflectance and atmospheric conditions as mentioned in Eq. 4 (Vermote et al., 1997). The model only requires a

minimal amount of input data and characteristics to provide this information. In the absence of atmospheric influences, the surface reflectance (Ref) is calculated as:

$$\text{Ref} = \frac{(A_{Aref} + B)}{[1 + (\gamma(A_{Aref} + B))]} \quad (10)$$

where $A = 1/\alpha\beta$, $B = A_{ref}/\beta$, α is the global gas transmittance, β is the total scattering transmittance, and γ is the spherical albedo (Mahiny and Turner, 2007). α , β , and γ are the constants generated from running the model.

FLAASH (Fast Line-of-sight Atmospheric Analysis of Spectral Hypercubes) Method

The physics-based radiative transfer model used in FLAASH is derived from MODTRAN4 (Matthew et al., 2002; Cooley et al., 2002; Berk et al., 1999). It is a great solution for atmospheric correction and can fix the cascade effect brought on by diffused reflection (Wang et al., 2018). Initial visibility (36.61 km) from Eq. 11, AOD at 550 nm of 0.273, and angstrom exponent of 0.471 are the atmospheric characteristics used for the FLAASH atmospheric algorithm in this work. The aerosol model is taken as rural, the altitude is 705 km, and the atmospheric model type is tropical. The surface reflectance image is the FLAASH algorithm result derived from the following mathematical expression:

$$\text{Visibility} = \frac{-15 \ln(ta(I)^\alpha)}{0.613} \quad (11)$$

$ta(I) = \text{AOD at 550 nm.}$

$\alpha = \text{angstrom exponent.}$

Result

The identification and mapping of land resources, such as vegetation and snow cover, is examined in this study using eight atmospheric correction methods that broadly fall under image-based and physics-based techniques. A visual comparison of the eight different types of atmospheric correction methods used on the Landsat 8 OLI in the snow and vegetation cover with and without the use of SHV (starting haze value) was done in the first stage. In contrast to the original Landsat 8 OLI image in DN (Digital Number), the brightness value of atmospherically corrected images is variable according to the parameter used in each model to correct the atmospheric influences. The atmospherically corrected reflectance images are as shown in Fig. 4a–h after applying the histogram equalization image

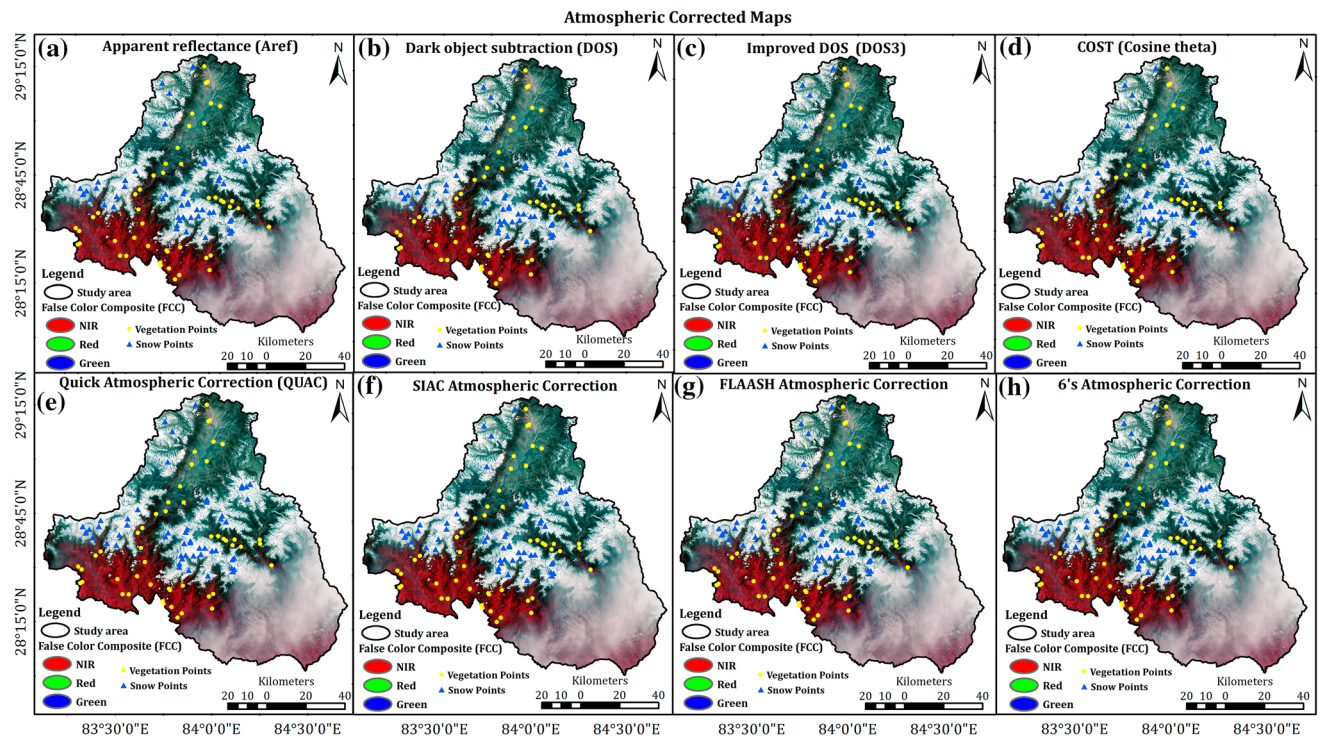


Fig. 4 The atmospherically corrected maps obtained **a** the apparent reflectance (Aref) method, **b** dark object subtraction (DOS) method; **c** improved dark object subtraction (DOS3) method; **d** Cosine theta (COST) method; **e** quick atmospheric correction (QUAC) method; **f** sensor invariant atmospheric correction (SIAC) method; **g** fast line-

of-sight atmospheric analysis of spectral hypercubes (FLAASH) method; and **h** second simulation of the satellite signal in the solar spectrum (6SV) method. The locations from where vegetation spectra were taken are shown in yellow dots, while the blue triangle shows the locations from where snow spectra were extracted

enhancement technique. The 50 random points each in vegetation and snow cover are also shown in Figs. 4a–h. These points are used to extract the reflectance values and then it was averaged for vegetation and snow cover across all atmospherically corrected images. The atmospheric correction techniques used are the most effective for reducing the attenuation of radiation caused by Rayleigh and Mie scattering in the upper atmosphere. These two scattering effects (hazy appearance) are clearly seen in the original image (Fig. 1c), while the adjusted haze effect in several atmospherically corrected images is shown in Figs. 4a–h. Table 3 displays the value of the specific scattering function that is used to eliminate haze effects from the original image. As we can see in Fig. 4, the hazy appearance due to Rayleigh and Mie scattering was corrected but the cloud remains unaltered with implemented different atmospheric correction methods.

Spectral Reflectance Curve

Spectral reflectance is the ratio of the amount of radiation returning from the Earth's surface to the amount of

radiation coming from the Earth's surface at a given spectral band (McCord et al., 1981). Reflectance is the unitless quantity that typically ranges between 0 and 1. By computing the mean of the reflectance measurements in the individual ranges, the spectral reflectance curve may be used to determine the total reflectance of selected pixels in each band. In this work, we explored the spectral signatures of snow and vegetation cover using the spectral profile tool in ENVI and compared them to the spectral libraries provided by the ENVI software.

Snow Reflectance Curve

The averaged snow reflectance curve is plotted as a function of wavelength. The snow spectral reflectance values extracted from different atmospherically corrected images are shown in 8 spectral profiles (Fig. 5). The spectral profile of snow shows “peak” and “valley” variations which is commonly utilized to compare the atmospheric correction methods. Snow reflects up to 95% of the entire visible light and 50–80% of incoming NIR light (Feister & Grewe, 1995). For all the atmospheric correction methods,

Fig. 5 The snow-covered spectral reflectance curve, which was extracted from eight different atmospheric correction techniques

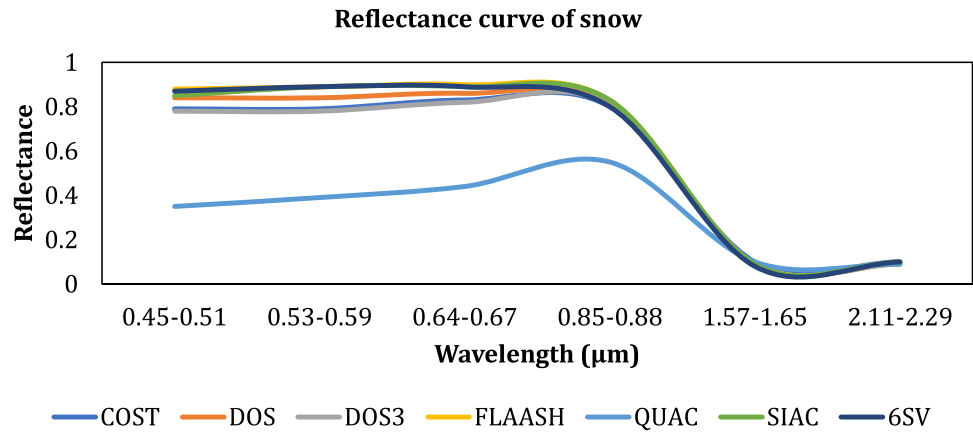


Table 4 The correlation of snow spectral values extracted from atmospherically adjusted images and standard spectral library. Their rank in the order of correlation is also shown

S.No	Correlation	Aref	COST	DOS	DOS3	FLAASH	QUAC	SIAC	6SV
1	Snow_Ref	1.00	0.99	1.00	0.99	1.00	0.90	1.00	1.00
2	Rank	4	6	3	7	2	8	5	1

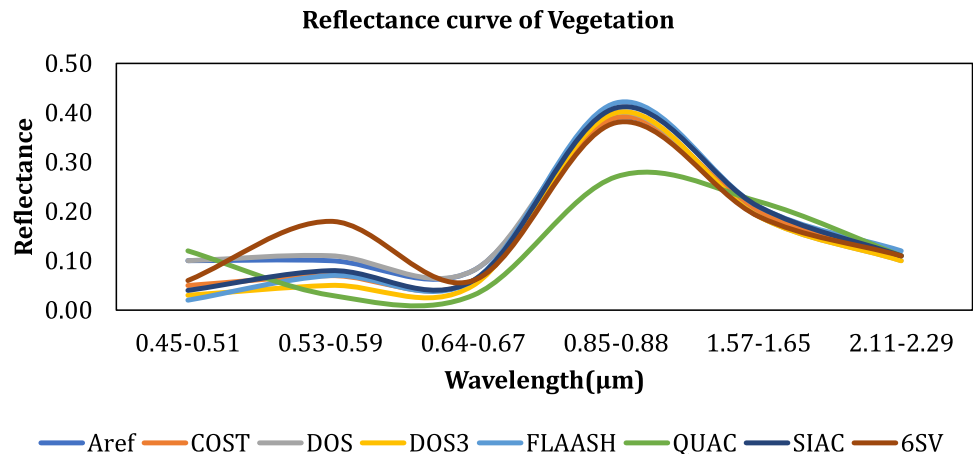
the reflectance of snow is higher in the visible region (blue (B), green (G), and red (R) bands), while the reflectance of the NIR bands is slightly lower, and the reflectance of the selected Landsat 8 SWIR1, SWIR2 bands is completely lower (Fig. 5).

The reflectance values of snow-covered areas, determined by the FLAASH approach are higher in the visible range (0.88, 0.89, and 0.9 for B, G, R, respectively) and comparatively lower in NIR wavelengths (0.83) as shown in Fig. 5 and Appendix 2, while QUAC technique exhibits lowest reflectance values in the visible (B, G, R: 0.35, 0.39, 0.44), and NIR (0.55) bands. Better snow spectral reflectance was also observed using the SIAC (B, G, R: 0.85, 0.89, 0.89; NIR:

0.83) and 6SV (B, G, R: 0.87, 0.89, 0.89; NIR: 0.8) method after FLAASH. Also, the snow spectral reflectance determined by DOS (B, G, R: 0.84, 0.84, 0.86; NIR: 0.81), COST (B, G, R: 0.79, 0.79, 0.83; NIR: 0.8), DOS3 (B, G, R: 0.78, 0.78, 0.82; NIR: 0.81), and Aref (B, G, R: 0.84, 0.82, 0.89; NIR: 0.85) are showing a decreased reflectivity (Appendix 2).

The snow spectral reflectance values calculated from atmospherically corrected Landsat 8 OLI images are compared with spectral libraries made available by ENVI (Table 4). The correlation values of snow spectra between the standard spectral library and the 6SV, SIAC, FLAASH, DOS, and Aref derived spectra are very high ($r^2 = 1$), while the correlation values with COST, DOS3, and QUAC

Fig. 6 The spectral reflectance curve of vegetation cover that was estimated using eight different atmospheric correction methods



are 0.99, 0.99, and 0.90, respectively, as shown in Table 4. Thus, 6SV has the highest rank of 1 (Table 4), followed by FLAASH with a rank of 2. The lowest ranks are obtained for DOS3 and QUAC, with ranks of 7 and 8, respectively.

Vegetation Reflectance Curve

The averaged vegetation reflectance curve is displayed as a function of wavelength. The vegetation spectral reflectance values extracted from different atmospherically corrected images are shown in 8 spectral profiles (Fig. 6).

The spectral profile of healthy green vegetation shows “crest” and “trough” variations which are commonly utilized to compare the atmospheric correction methods. The wavelength area visible (B, G, R), near-infrared (NIR), and beyond shortwave infrared (SWIR) can all be examined separately. In the visible region (0.4–0.7 μm), healthy vegetation generally absorbs the electromagnetic energy, while in the red/infrared boundary around 0.7 μm , absorption drastically decreases, and reflection increases. From 0.7 to 1.3 μm , the reflectance is almost constant, and at longer wavelengths, it starts to decline as shown in Fig. 6. Hence for further analysis spectral reflectance values at the NIR band were considered for comparison.

It is observed that the NIR wavelengths showed the highest reflectance value (0.42) for vegetated areas when corrected using FLAASH setting (Appendix 3), while the lowest reflectance value (0.27) in the NIR band for the same pixels is obtained in the QUAC corrected image, as shown in Appendix 3 and Fig. 6. After that, the improved vegetation spectral reflectance was seen with the SIAC (0.41), DOS (0.40), and DOS3 (0.40) approaches. As seen in Appendix 3, the spectral reflectance for vegetation areas, as measured by Aref (0.39), COST (0.39), and 6SV (0.38), has indicated decreased spectral reflectance.

The values of vegetation spectral reflectance derived from atmospherically corrected Landsat 8 OLI images are compared with spectral libraries made accessible by ENVI, as shown in Table 5. Higher correlation values are obtained for 6SV, SIAC, COST, DOS3, and Aref having $r^2 = 1$, whereas the correlation values for the FLAASH and QUAC are, respectively, 0.99 and 0.87. In Table 5, it is evident that COST has the highest rank, which is 1, followed by

6SV, which has a rank of 2. The DOS and QUAC represent the lowest ranks with values 7 and 8 respectively as shown in Table 5.

Statistical Analysis

The statistical mean (μ) is derived from the snow reflectance data for each atmospherically corrected Landsat 8 OLI image Table 6. The 6SV (μ :0.61), SIAC (μ :0.61), and FLAASH (μ :0.62) techniques have similar means. This explains that the results of these three atmospheric correction techniques were comparable in terms of the information content for the snow cover areas. Similarly, Table 6 shows that the mean snow reflectance generated by QUAC has a lower mean value (0.32). The FLAASH, SIAC, and 6SV methods produce higher snow mean reflectance values when compared to other image-based correction techniques (Aref, COST, DOS, DOS3). This suggests that, when compared to other atmospheric correction techniques, FLAASH, SIAC, and 6SV approaches are better for atmospheric correction and have a high possibility of delivering true snow features from Landsat 8 OLI.

Similarly, the statistical mean (μ) was obtained for the vegetation reflectance value for each atmospherically corrected Landsat 8 OLI image (Table 7). The higher mean reflectance values for vegetation are observed for the 6SV (μ :0.21), FLAASH (μ :0.20), and SIAC (μ :0.19) methods. This indicates that in terms of the information content of the vegetation cover, the mean values of these three atmospheric correction methods were similar. Table 7 demonstrates that the mean vegetation reflectance value produced by QUAC is the lowest (0.13). In comparison to other image-based correction methods (Aref, COST, DOS, DOS3), as shown in Table 7, the FLAASH, SIAC, and 6SV methods produce higher mean vegetation reflectance values. Thus, FLAASH, SIAC, and 6SV methods offer a high chance of providing accurate vegetation information from Landsat 8 OLI.

Normalized Difference Snow Index (NDSI)

NDSI is a semi-automated technique for extracting ice (snow) from satellite images. For the Landsat 8 OLI band,

Table 5 The correlation of vegetation spectral values extracted from atmospherically adjusted images and standard spectral library. Their rank in the order of correlation is also shown

S.No	Correlation	Aref	COST	DOS	DOS3	FLAASH	QUAC	SIAC	6S
1	Vegetation_Ref	1.00	1.00	0.99	1.00	0.99	0.87	1.00	1.00
2	Rank	5.00	1.00	7.00	4.00	6.00	8.00	3.00	2.00

Table 6 The mean of the snow cover reflectance values that are obtained from all the atmospheric correction methods

Method	Aref	COST	DOS	DOS3	FLAASH	QUAC	SIAC	6S
Mean	0.58	0.57	0.58	0.56	0.62	0.32	0.61	0.61

Table 7 The mean of the vegetation cover reflectance values that are obtained from all the atmospheric correction methods

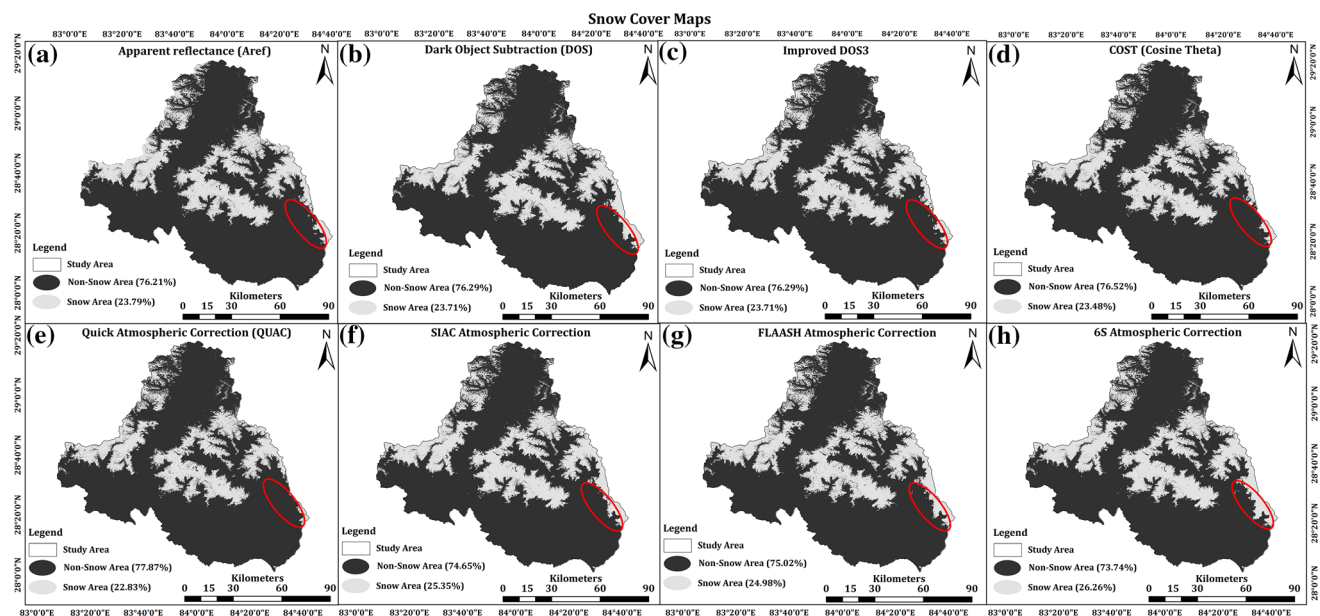
Method	Aref	COST	DOS	DOS3	FLAASH	QUAC	SIAC	6S
Mean	0.16	0.15	0.16	0.14	0.2	0.13	0.19	0.21

it is the ratio of visible (Green) to SWIR1 band. The spectral information available in the (Green, SWIR1) plays an important role in using NDSI to map the snow area on the earth's surface. The following equation (Burns et al., 2014) denotes the mathematical expression of NDSI for Landsat 8 OLI:

$$\text{NDSI} = \frac{(\text{Green} - \text{SWIR1})}{(\text{Green} + \text{SWIR1})} \quad (12)$$

Snow features had the highest reflectance in the visible and NIR bands and the lowest reflectance in the SWIR1 and SWIR2 bands in all the atmospheric corrected images, as illustrated in Fig. 5. This is extremely helpful in the utilization of NDSI for snow cover mapping. It can also reduce the effects of topography, allowing features beneath high mountain shadows to be well distinguished. A

threshold on NDSI is applied to identify snow and non-snow areas. NDSI thresholding is the most vital phase in snow cover demarcation and mapping because it determines the most ideal value from the NDSI stated range. It is the process of separating and segmenting continuous (greyscale) data into discrete (thematic) data. In this study, several threshold values were applied for extracting snow from atmospherically corrected images that match the earth's surface. The histogram-based thresholding is useful for identifying the spread of NDSI values (e.g., normal distribution, negative or positively skewed distribution, multimodal or uniform distribution). The histogram technique of NDSI thresholding is a standard way of segmenting and mapping snow and non-snow areas. The NDSI was used to detect snow in snow-covered forest areas, with the NDSI threshold value set to 0.4, based on the statistical

**Fig. 7** The snow cover maps obtained from NDSI thresholding for eight different atmospheric correction methods. The red ellipse shows the areas where changes are visible among all the output images

results. The histogram threshold value is chosen to be > 0.4 of the calculated NDSI.

Snow Cover Maps (SCM)

The snow cover maps were prepared for various atmospherically corrected reflectance images that categorize into two classes, namely snow and non-snow areas represented by white and black, as shown in Fig. 7. The 6SV atmospheric corrected image covered a greater snow area (26.26%), followed by the SIAC (25.35%) and FLAASH (24.98%) methods. The QUAC method of atmospheric correction has shown a lesser snow cover area of 22.83% as compared to other corrected reflected images as shown in Fig. 7, while Aref, DOS, DOS3, and COST methods have shown 23.79%, 23.71%, 23.71%, and 23.48% snow area, respectively, which is less than the snow cover area calculated by 6SV, SIAC, and FLAASH atmospheric correction methods. Some variations in the snow cover area are seen in Fig. 7a–h, lower-right corner, which is denoted with a red ellipse. This is the same area that is obscured by a thin cloud cover as shown in Fig. 2. This indicates that the 6SV, SIAC, and FLAASH method function satisfactorily, when compared to other methods, to extract the snow area covered by a thin cloud cover and haze as shown in Fig. 7, while other methods like Aref, DOS, DOS3, QUAC, and COST do not perform well in extracting the information that is obscured by thin cloud cover and haze in the study area.

Normalized Difference Vegetation Index (NDVI)

The Normalized Difference Vegetation Index (NDVI) is commonly used to determine the area of vegetation cover all over the world. The NDVI is the ratio of the difference in reflectance in the Near-Infrared (NIR) and Red bands to the sum of these two bands and is given as (Kaufman & Holben, 1993):

$$\text{NDVI} = \frac{(\text{NIR} - \text{RED})}{(\text{NIR} + \text{RED})} \quad (13)$$

The value of NDVI varies from -1 to 1 , which is generally classified as:

NDVI = -1 to 0 represents water bodies that do not reflect much in either red or NIR bands.

NDVI = -0.1 to 0.1 represent barren rocks, sand, or snow.

NDVI = 0.2 to 0.4 represent agriculture.

NDVI = $0.5-1$ represents healthy vegetation (Crippen, 1990) due to very high reflectance in the NIR band.

NDVI clearly distinguishes vegetation from other features in the satellite image even in the presence of thin cloud cover, topography effects, and haze (Pettorelli, 2013). As shown in Fig. 6, the spectral reflectance curve of healthy green vegetation exhibits a minimum reflectance in the visible region (RGB) of the electromagnetic spectrum due to the pigments in plant leaves. In the reflective near-infrared region (NIR), reflectance increases a lot. Therefore, in all atmospheric correction methods, vegetation features had the lowest reflectance in the visible wavelengths and the highest reflectivity in the NIR band, as seen in Fig. 6. For mapping vegetation cover, this is extremely useful in generating NDVI.

After computing NDVI indices, the most crucial step in delineating and mapping vegetation cover is NDVI thresholding, which selects the most ideal value from the NDVI given range. In this study, multiple threshold values were applied for the extraction of vegetation cover from atmospherically corrected images. Finally, a histogram thresholding method based on mean NDVI values is chosen for mapping vegetative cover from the various atmospherically corrected reflected images.

Vegetation Cover Maps (VCM)

The study area was divided into two categories, i.e., vegetation and non-vegetation areas, represented as green and black, respectively, while creating the vegetation cover maps for various atmospherically corrected reflectance images as shown in Fig. 8. It was observed that in the 6SV atmospheric corrected image, larger area (35.79%) is categorized as vegetation as compared to that of SIAC (35.73%) and FLAASH (34.09%) methods. In comparison to other corrected reflected images, the Aref method covered the least vegetation area of 30.39%, as seen in Fig. 8, whereas other methods like COST (34.92%), QUAC (33.29%), DOS (30.64%), and DOS3 (31.86%) did cover a lesser area as vegetation. There are certain areas where changes in the vegetation cover area are seen, which are highlighted in the red circle as shown in Fig. 8a–h. These are similar locations where thin cloud is present as seen in Fig. 2. This demonstrates that, when compared to other methods, the FLAASH, SIAC, and 6SV methods acceptably extract the vegetation area covered by thin cloud cover, and haze that other methods could not extract.

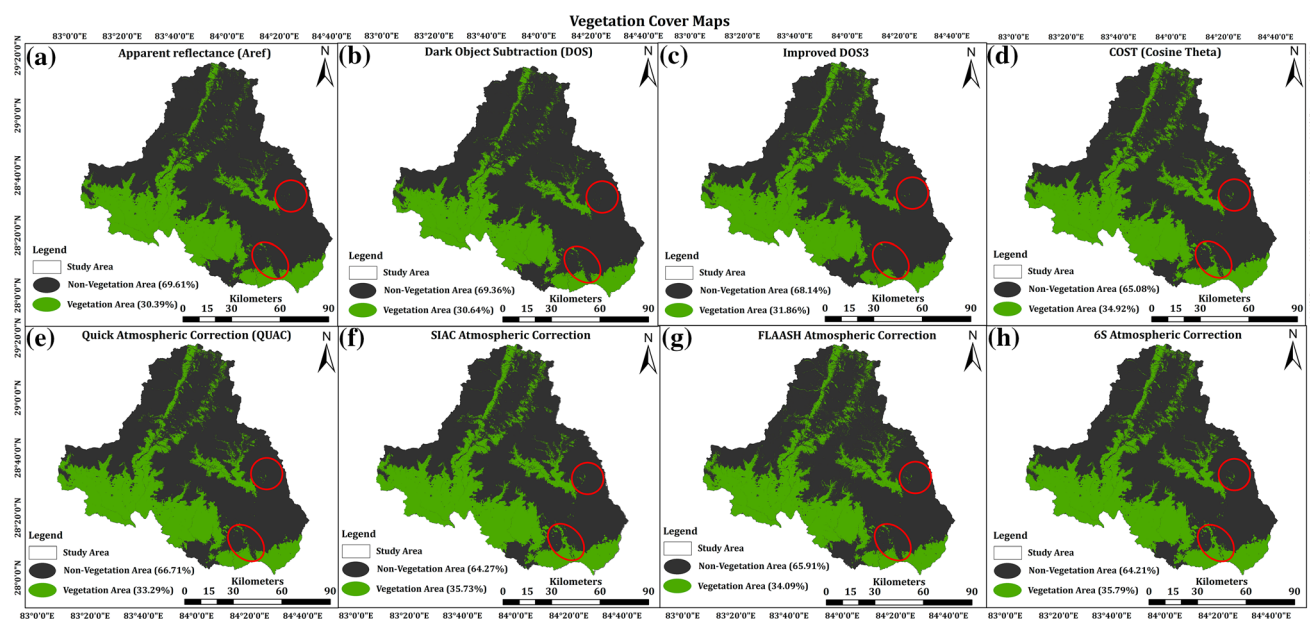


Fig. 8 The vegetation cover maps obtained from NDVI thresholding for eight different atmospheric correction methods. The areas where changes are visible are marked in red circle/ellipse

Discussion

Many authors tried to compare the effects of different atmospheric correction methods, including both image-based and physics-based, with the field observed spectral reflectance data. Different methods that have been employed are DOS, COST, ELM, ATCOR, QUAC, 6SV, and FLAASH (Nazeer et al., 2014; Mandanici et al., 2015; Marcello et al., 2016; Peng et al., 2016; Eugenio et al., 2017; Wang et al., 2018). In addition to similar work some authors compared the results of atmospheric corrections among themselves and with different indices such as NDVI, NDSI, SAVI, etc. (Mandanici et al., 2015; Kaneko et al., 2016; Lhissou et al., 2020; Moravec et al., 2021; Jasrotia et al., 2022). In most of the published literature, it was observed that physics-based atmospheric correction methods outperforms the image-based atmospheric correction methods.

The results obtained from two physics-based methods (FLAASH and 6SV) differ significantly from those of the image-based methods (QUAC, DOS1), while they are in good agreement with one another (Mandanici et al., 2015). When using FLAASH and 6S atmospheric corrections methods, very minor discrepancies were obtained (Moravec et al., 2021). It was concluded that physics-based atmospheric correction methods correctly corrected the atmospheric disturbances (Eugenio et al., 2017; Wang

et al., 2018), mainly in the vegetation and soil areas from several protected semi-arid environments (high mountain and coastal areas) (Marcello et al., 2016); over Chinese forest, grassland, and desert areas (Xie et al., 2010; Peng et al., 2016). The main reason for better performance of physics-based methods is precise estimation of path radiance and precise recovery of the earth's surface reflectance than the image-based method, especially in vegetation areas (Kaneko et al., 2016). As a result, the 6SV method of atmospheric correction was closest to the ground spectral reflectance values (Xie et al., 2010; Nazeer et al., 2014; Peng et al., 2016). The spectral reflectance is overestimated by the physics-based method throughout all spectral bands, while it is significantly underestimated by the image-based methods (empirical method), particularly in the visible region of the electromagnetic spectrum (Mandanici et al., 2015). In conclusion, physics-based methods, particularly 6SV, have showed better performance, achieving reflectance estimations that are extremely close to the in-situ data (Marcello et al., 2016). Similar results are obtained in this work where physics-based atmospheric correction methods showed better results than the image-based atmospheric correction methods. Particularly, we observed good results while using FLAASH, SIAC and 6SV method in the mountainous region of Nepal Himalayas.

We observed that there is an increase of reflectivity in the near-infrared region and decrease of reflectivity in the

visible region after applying several atmospheric corrections methods on Landsat 8 OLI images. Similar pattern as also observed for a study carried out in Spain using Sentinel-2 satellite data (Valdivieso-Ros et al., 2021). The changes in RED and NIR bands that are used for NDVI calculation were observable, but their histogram shape was similar to that of the top of the atmosphere image. However, we found that QUAC atmospheric corrected image was the worst as also reported by Moravec et al., (2021). They found that the surface reflectance of RED and NIR bands was shifted for QUAC method in comparison to the other atmospheric correction methods while applying the correction methods on Sentinel-2 and Landsat 8 images (Moravec et al., 2021). There were certain locations where thin cloud was present in our study area which decreased the NDVI and NDSI area for original and other image-based correction methods. However, some of these snow and vegetation areas were better represented using the physics-based atmospheric correction methods mainly FLAASH and 6SV followed by SIAC. Higher values for maximum NDSI and NDVI were obtained in atmospheric corrected Landsat 8 images of Jhelum Basin, Western Himalaya (Jasrotia et al., 2022).

Conclusion

In this work, eight atmospheric correction methods, including 5 image-based and 3 physics-based models, are applied on Landsat 8 OLI satellite image to assess the best model for mapping snow and vegetation covered areas. The original Landsat 8 OLI was successfully corrected using the DOS, DOS3, COST, Aref, QUAC, SIAC, FLAASH, and 6SV atmospheric correction methods. The reflectance values of the snow and vegetation covered 50 pixels were extracted from all the corrected reflectance images. These derived snow and vegetation reflectance spectra were compared with the standard spectra from the ENVI software's spectral library. In comparison to all the applied methods, the FLAASH (B, G, R: 0.88, 0.89, 0.9; NIR: 0.83), SIAC (B, G, R: 0.85, 0.89, 0.89; NIR: 0.83) and 6SV

(B, G, R: 0.87, 0.89, 0.89; NIR:0.8) methods determined the better snow reflectance values. The 6SV technique received the highest rank of 1 followed by FLAASH method for best correlation of snow reflectance with the standard reflectance, whereas DOS3 and QUAC methods were the worst. In the NIR band, the FLAASH and SIAC methods show greater vegetation reflectance values than other methods. But in terms of rank while correlating the extracted vegetation spectra with the standard spectra, the COST technique has a rank of 1, which is the highest, and 6SV is ranked second, while DOS and QUAC obtained a rank of 7 and 8. In this study, we found that when compared to other image-based correction methods (QUAC, Aref, COST, DOS, and DOS3), the FLAASH, SIAC, and 6SV methods generate higher snow and vegetation mean reflectance values, thus having a high possibility of mapping true snow and vegetation features. The snow and vegetation cover maps produced from all atmospherically corrected reflected images demonstrated that, FLAASH, SIAC, and 6SV methods could extract the underneath information from the area covered by thin cloud cover, and haze.

As QUAC, DOS, DOS3, and COST methods could correct for hazy appearance caused by dark objects, they depend on the accuracy of the system's gain and offset as well as the addition of a term to account for atmospheric transmittance, which has a multiplicative effect rather than an additive one, whereas FLAASH, 6SV, and SIAC, on the other hand, are based on radiative transfer models and take the radiation transmission process in the range of visible light to the SWIR band into consideration. They describe the state of the radiation source, the atmosphere (including Rayleigh scattering, aerosol scattering, and vapor absorption), and the sensor's geometrical parameters.

Appendix 1

See Table 8.

Table 8 The gain and bias value used during DN to radiance conversion

S.No	Bands	Gain	Bias
1	Band 2-Blue	0.013	– 64.336
2	Band 3-Green	0.012	– 59.285
3	Band 4-Red	0.010	– 49.992
4	Band 5-Near-Infrared (NIR)	0.006	– 30.593
5	Band 6-Shortwave Infrared (SWIR) 1	0.002	– 7.608
6	Band 7-Shortwave Infrared (SWIR) 2	0.001	– 2.564

Appendix 2

See Table 9.

Table 9 Snow spectral reflectance determined from eight different atmospheric correction methods along with the standard snow spectral reflectance taken from USGS library as provided in the ENVI spectral libraries

Bands	Wavelength(μm)	USGS Spectral Library Snow_Ref	Reflectance(0–1)							
			Aref	COST	DOS	DOS3	FLAASH	QUAC	SIAC	6SV
Blue	0.45–0.51	0.72	0.84	0.79	0.84	0.78	0.88	0.35	0.85	0.87
Green	0.53–0.59	0.72	0.82	0.79	0.84	0.78	0.89	0.39	0.89	0.89
Red	0.64–0.67	0.71	0.85	0.83	0.86	0.82	0.9	0.44	0.89	0.89
NIR	0.85–0.88	0.64	0.8	0.8	0.81	0.81	0.83	0.55	0.83	0.8
SWIR1	1.57–1.65	0.11	0.09	0.1	0.09	0.09	0.09	0.1	0.09	0.08
SWIR2	2.11–2.29	0.08	0.09	0.1	0.09	0.09	0.1	0.09	0.1	0.1

Appendix 3

See Table 10.

Table 10 Vegetation spectral reflectance determined from eight different atmospheric correction methods along with the standard vegetation spectral reflectance taken from USGS library as provided in the ENVI spectral libraries

Bands	Wavelength(μm)	USGS Spectral Library Snow_Ref	Reflectance(0–1)							
			Aref	COST	DOS	DOS3	FLAASH	QUAC	SIAC	6S
Blue	0.45–0.51	0.72	0.84	0.79	0.84	0.78	0.88	0.35	0.85	0.87
Green	0.53–0.59	0.72	0.82	0.79	0.84	0.78	0.89	0.39	0.89	0.89
Red	0.64–0.67	0.71	0.85	0.83	0.86	0.82	0.9	0.44	0.89	0.89
NIR	0.85–0.88	0.64	0.8	0.8	0.81	0.81	0.83	0.55	0.83	0.8
SWIR1	1.57–1.65	0.11	0.09	0.1	0.09	0.09	0.09	0.1	0.09	0.08
SWIR2	2.11–2.29	0.08	0.09	0.1	0.09	0.09	0.1	0.09	0.1	0.1

Acknowledgements The opportunity and technology resources for the authors to conduct this study are provided by IIT Mandi in Kamand, Himachal Pradesh, India. Additionally, we appreciate the USGS's Land Processes Distributed Active Archive Center (LP DAAC) for allowing us to use the Landsat 8 OLI datasets in this study. The authors are grateful for the anonymous reviewers' suggestions, which helped to refine the manuscript and make it more presentable.

Funding This research article received no specific grant from any funding organization/ institution.

Declarations

Conflict of interest The authors claim that they have no known financial conflicts of interest or close personal relationships that would have affected the work presented in this study.

References

- Andreassen, L. M., Paul, F., Kääb, A., & Hausberg, J. E. (2008). Landsat-derived glacier inventory for Jotunheimen, Norway, and deduced glacier changes since the 1930s. *The Cryosphere*, 2(1), 131–145.
- Asra, G. (1989). Theory and applications of optical remote sensing. In G. Asrar (Ed.) New York: Wiley.
- Baisantry, M., Negi, S., & Manocha, O. P. (2012). Automatic relative radiometric normalization for change detection of satellite imagery. *ACEEE International Journal on Information Technology*, 2(2), 28–31.
- Barnas, A. F., Darby, B. J., Vandeberg, G. S., Rockwell, R. F., & Ellis-Felege, S. N. (2019). A comparison of drone imagery and ground-based methods for estimating the extent of habitat destruction by lesser snow geese (*Anser caerulescens caerulescens*) in La Pérouse Bay. *PLoS ONE*, 14(8), e0217049.
- Basith, A., Nuha, M. U., Prastyani, R., & Winarso, G. (2019). Aerosol optical depth (AOD) retrieval for atmospheric correction in Landsat-8 imagery using second simulation of a satellite signal

- in the solar spectrum-vector (6SV). *Communications in Science and Technology*, 4(2), 68–73.
- Basnet, K., Paudel, R. C., & Sherchan, B. (2019). Analysis of watersheds in Gandaki Province. *Nepal Using QGIS. Technical Journal*, 1(1), 16–28.
- Berk, A., Anderson, G. P., Bernstein, L. S., Acharya, P. K., Dothe, H., Matthew, M. W., & Hoke, M. L. (1999). MODTRAN4 radiative transfer modeling for atmospheric correction. In *Optical spectroscopic techniques and instrumentation for atmospheric and space research III*, 3756, 348–353.
- Bernstein, L. S., Adler-Golden, S. M., Sundberg, R. L., Levine, R. Y., Perkins, T. C., Berk, A., & Hoke, M. L. (2005). Validation of the QUick atmospheric correction (QUAC) algorithm for VNIR-SWIR multi-and hyperspectral imagery. In *Algorithms and Technologies for Multispectral, Hyperspectral, and Ultraspectral Imagery XI*, 5806, 668–678.
- Bernstein, L. S., Jin, X., Gregor, B., & Adler-Golden, S. M. (2012). Quick atmospheric correction code: Algorithm description and recent upgrades. *Optical Engineering*, 51(11), 111719.
- Bhambri, R., Bolch, T., & Chaujar, R. K. (2011). Mapping of debris-covered glaciers in the Garhwal Himalayas using ASTER DEMs and thermal data. *International Journal of Remote Sensing*, 32(23), 8095–8119.
- Burns, P., & Nolin, A. (2014). Using atmospherically-corrected Landsat imagery to measure glacier area change in the Cordillera Blanca, Peru from 1987 to 2010. *Remote Sensing of Environment*, 140, 165–178.
- Caselles, V., & Lopez Garcia, M. J. (1989). An alternative simple approach to estimate atmospheric correction in multitemporal studies. *International Journal of Remote Sensing*, 10(6), 1127–1134.
- Chavez, P. S., Jr. (1989). Radiometric calibration of Landsat Thematic Mapper multispectral images. *Photogrammetric Engineering and Remote Sensing*, 55(9), 1285–1294.
- Chavez, P. S. (1996). Image-based atmospheric corrections-revisited and improved. *Photogrammetric Engineering and Remote Sensing*, 62(9), 1025–1035.
- Chen, W., Chen, W., & Li, J. (2010). Comparison of surface reflectance derived by relative radiometric normalization versus atmospheric correction for generating large-scale Landsat mosaics. *Remote Sensing Letters*, 1(2), 103–109.
- Cooley, T., Anderson, G. P., Felde, G. W., Hoke, M. L., Ratkowski, A. J., Chetwynd, J. H., & Lewis, P. (2002). FLAASH, a MODTRAN4-based atmospheric correction algorithm, its application and validation. In *IEEE international geoscience and remote sensing symposium*, 3, 1414–1418.
- Crippen, R. E. (1988). The dangers of underestimating the importance of data adjustments in band ratioing. *Remote Sensing*, 9(4), 767–776.
- Crippen, R. E. (1990). Calculating the vegetation index faster. *Remote Sensing of Environment*, 34(1), 71–73.
- Cui, L., Li, G., Ren, H., He, L., Liao, H., Ouyang, N., & Zhang, Y. (2014). Assessment of atmospheric correction methods for historical Landsat TM images in the coastal zone: A case study in Jianguo, China. *European Journal of Remote Sensing*, 47(1), 701–716.
- Domenikiotis, C., Loukas, A., & Dalezios, N. R. (2003). The use of NOAA/AVHRR satellite data for monitoring and assessment of forest fires and floods. *Natural Hazards and Earth System Sciences*, 3(1/2), 115–128.
- Eugenio, F., Marcello, J., Martin, J., & Rodríguez-Esparragón, D. (2017). Benthic habitat mapping using multispectral high-resolution imagery: Evaluation of shallow water atmospheric correction techniques. *Sensors*, 17(11), 2639.
- Feister, U., & Grewe, R. (1995). Spectral albedo measurements in the UV and visible region over different types of surfaces. *Photochemistry and Photobiology*, 62(4), 736–744.
- Gupta, S. K., & Shukla, D. P. (2020). Evaluation of topographic correction methods for LULC preparation based on multi-source DEMs and Landsat-8 imagery. *Spatial Information Research*, 28(1), 113–127.
- Hall, F. G., Strebel, D. E., Nickeson, J. E., & Goetz, S. J. (1991). Radiometric rectification: Toward a common radiometric response among multirate, multisensor images. *Remote Sensing of Environment*, 35(1), 11–27.
- Huete, A., Justice, C., & Van Leeuwen, W. (1999). MODIS vegetation index (MOD13). *Algorithm Theoretical Basis Document*, 3(213), 295–309.
- Jasrotia, A. S., Kour, R., & Ashraf, S. (2022). Impact of illumination gradients on the raw, atmospherically and topographically corrected snow and vegetation areas of Jhelum basin, Western Himalayas. *Geocarto International*. <https://doi.org/10.1080/10106049.2022.2086629>
- Jensen, J. R. (2009). Remote sensing of the environment: An earth resource perspective 2/e. Pearson Education India.
- Kaneko, E., Aoki, H., Tsukada, M. (2016). Image-based path radiance estimation guided by physical model. In *2016 IEEE International Geoscience and Remote Sensing Symposium (IGARSS)* pp. 6942–6945. IEEE.
- Kaufman, Y. J. (1989). The atmospheric effect on remote sensing and its correction. *Theory and Application of Optical Remote Sensing*, 336–428.
- Kaufman, Y. J., & Holben, B. N. (1993). Calibration of the AVHRR visible and near-IR bands by atmospheric scattering, ocean glint and desert reflection. *International Journal of Remote Sensing*, 14(1), 21–52.
- Kaushik, S., Joshi, P. K., & Singh, T. (2019). Development of glacier mapping in Indian Himalaya: A review of approaches. *International Journal of Remote Sensing*, 40(17), 6607–6634.
- Kim, M., Heo, J. H., & Sohn, E. H. (2022). Atmospheric correction of true-color RGB imagery with limb area-blending based on 6S and satellite image enhancement techniques using geo-kompsat-2A advanced meteorological imager data. *Asia-Pacific Journal of Atmospheric Sciences*, 58(3), 333–352.
- Lhissou, R., El Harti, A., Maimouni, S., & Adiri, Z. (2020). Assessment of the image-based atmospheric correction of multispectral satellite images for geological mapping in arid and semi-arid regions. *Remote Sensing Applications: Society and Environment*, 20, 100420.
- Liou, K. N. (2002). *An introduction to atmospheric radiation*. Elsevier.
- López-Serrano, P. M., Corral-Rivas, J. J., Díaz-Varela, R. A., Álvarez-González, J. G., & López-Sánchez, C. A. (2016). Evaluation of radiometric and atmospheric correction algorithms for aboveground forest biomass estimation using Landsat 5 TM data. *Remote Sensing*, 8(5), 369.
- Lu, D., Mausel, P., Brondizio, E., & Moran, E. (2002). Assessment of atmospheric correction methods for Landsat TM data applicable to Amazon basin LBA research. *International Journal of Remote Sensing*, 23(13), 2651–2671.
- Mahiny, A. S., & Turner, B. J. (2007). A comparison of four common atmospheric correction methods. *Photogrammetric Engineering & Remote Sensing*, 73(4), 361–368.
- Mandanici, E., Franci, F., Bitelli, G., Agapiou, A., Alexakis, D., & Hadjimitsis, D. G. (2015). Comparison between empirical and physically based models of atmospheric correction. In *Third International Conference on Remote Sensing and Geoinformation of the Environment (RSCy2015)*, Vol. 9535, pp. 110–119. SPIE.

- Marcello, J., Eugenio, F., Perdomo, U., & Medina, A. (2016). Assessment of atmospheric algorithms to retrieve vegetation in natural protected areas using multispectral high-resolution imagery. *Sensors*, 16(10), 1624.
- Matsushita, B., Yang, W., Chen, J., Onda, Y., & Qiu, G. (2007). Sensitivity of the enhanced vegetation index (EVI) and normalized difference vegetation index (NDVI) to topographic effects: A case study in high-density cypress forest. *Sensors*, 7(11), 2636–2651.
- Matthew, M. W., Adler-Golden, S. M., Berk, A., Felde, G., Anderson, G. P., Gorodetzky, D., Shippert, M. (2002). Atmospheric correction of spectral imagery: evaluation of the FLAASH algorithm with AVIRIS data. In Applied Imagery Pattern Recognition Workshop, 2002. Proceedings. pp. 157–163. IEEE.
- McCord, T. B., Clark, R. N., Hawke, B. R., McFadden, L. A., Owensby, P. D., Pieters, C. M., & Adams, J. B. (1981). Moon: Near-infrared spectral reflectance, a first good look. *Journal of Geophysical Research: Solid Earth*, 86(B11), 10883–10892.
- Susan Moran, M., Jackson, R. D., Slater, P. N., & Teillet, P. M. (1992). Evaluation of simplified procedures for retrieval of land surface reflectance factors from satellite sensor output. *Remote Sensing of Environment*, 41(2–3), 169–184. [https://doi.org/10.1016/0034-4257\(92\)90076-V](https://doi.org/10.1016/0034-4257(92)90076-V)
- Moravec, D., Komárek, J., López-Cuervo Medina, S., & Molina, I. (2021). Effect of atmospheric corrections on NDVI: Intercomparability of Landsat 8, Sentinel-2, and UAV sensors. *Remote Sensing*, 13(18), 3550.
- Navalgund, R. R., Jayaraman, V., & Roy, P. S. (2007). Remote sensing applications: An overview. *Current Science* (00113891), 93(12), 1747–1766.
- Nazeer, M., Nichol, J. E., & Yung, Y. K. (2014). Evaluation of atmospheric correction models and Landsat surface reflectance product in an urban coastal environment. *International Journal of Remote Sensing*, 35(16), 6271–6291.
- Pant, R. R., Zhang, F., Rehman, F. U., Wang, G., Ye, M., Zeng, C., & Tang, H. (2018). Spatiotemporal variations of hydrogeochemistry and its controlling factors in the Gandaki River Basin, Central Himalaya Nepal. *Science of the Total Environment*, 622, 770–782.
- Paolini, L., Grings, F., Sobrino, J. A., Jiménez Muñoz, J. C., & Karszenbaum, H. (2006). Radiometric correction effects in Landsat multi-date/multi-sensor change detection studies. *International Journal of Remote Sensing*, 27(4), 685–704.
- Paul, F. (2000). Evaluation of different methods for glacier mapping using Landsat TM. *EARSeL eProceedings*, 1, 239–245.
- Peng, Y., He, G., Zhang, Z., Long, T., Wang, M., & Ling, S. (2016). Study on atmospheric correction approach of Landsat-8 imageries based on 6S model and look-up table. *Journal of Applied Remote Sensing*, 10(4), 045006.
- Pettorelli, N. (2013). *The normalized difference vegetation index*. Oxford University Press.
- Phillips, O. L. (1997). The changing ecology of tropical forests. *Biodiversity & Conservation*, 6(2), 291–311.
- Price, J. C. (1987). Calibration of satellite radiometers and the comparison of vegetation indices. *Remote Sensing of Environment*, 21(1), 15–27.
- Prosperi, P. (2012). Evaluation of a remote sensing based method for the assessment of agricultural crop residues on the soil surface. Tutor: S. Bocchi ; coordinatore G. Zocchi. - . Università degli Studi di Milano, 2012 Feb 10. ((24. ciclo, Anno Accademico 2011. [10.13130/prosperi-paolo_phd2012-02-10].
- Richards, J. A. (1993). Sources and characteristics of remote sensing image data. In J. A. Richards (Ed.), *Remote Sensing Digital Image Analysis* (pp. 1–37). Berlin, Heidelberg: Springer. https://doi.org/10.1007/978-3-642-88087-2_1
- Richter, R. (1996). Atmospheric correction of satellite data with haze removal including a haze/clear transition region. *Computers & Geosciences*, 22(6), 675–681.
- Sabins, F. F. (1987). Remote sensing—principles and interpretation. WH Freeman and company.
- Schroeder, T. A., Cohen, W. B., Song, C., Canty, M. J., & Yang, Z. (2006). Radiometric correction of multi-temporal Landsat data for characterization of early successional forest patterns in western Oregon. *Remote Sensing of Environment*, 103(1), 16–26.
- Selkowitz, D. J., & Forster, R. R. (2016). An automated approach for mapping persistent ice and snow cover over high latitude regions. *Remote Sensing*, 8(1), 16.
- Slater, P. N. (1985). Radiometric considerations in remote sensing. *Proceedings of the IEEE*, 73(6), 997–1011.
- Song, C., Woodcock, C. E., Seto, K. C., Lenney, M. P., & Macomber, S. A. (2001). Classification and change detection using Landsat TM data: When and how to correct atmospheric effects? *Remote Sensing of Environment*, 75(2), 230–244.
- Thorne, K., Markham, B., Barker, P. S., & Biggar, S. J. P. E. (1997). Radiometric calibration of Landsat. *Photogrammetric Engineering & Remote Sensing*, 63(7), 853–858.
- Valdivieso-Ros, C., Alonso-Sarria, F., & Gomariz-Castillo, F. (2021). Effect of different atmospheric correction algorithms on sentinel-2 imagery classification accuracy in a semiarid mediterranean area. *Remote Sensing*, 13(9), 1770.
- Vermote, E. F., Tanré, D., Deuze, J. L., Herman, M., & Morcette, J. J. (1997). Second simulation of the satellite signal in the solar spectrum, 6S: An overview. *IEEE Transactions on Geoscience and Remote Sensing*, 35(3), 675–686.
- Wang, D., Ma, R., Xue, K., & Loiselle, S. A. (2019). The assessment of Landsat-8 OLI atmospheric correction algorithms for inland waters. *Remote Sensing*, 11(2), 169.
- Wang, Z., Xia, J., Wang, L., Mao, Z., Zeng, Q., Tian, L., & Shi, L. (2018). Atmospheric correction methods for GF-1 WFV1 data in hazy weather. *Journal of the Indian Society of Remote Sensing*, 46(3), 355–366.
- Xie, Y., Zhao, X., Li, L., Wang, H. (2010). Calculating NDVI for Landsat7-ETM data after atmospheric correction using 6S model: A case study in Zhangye city, China. In 2010 18th International Conference on Geoinformatics (pp. 1–4). IEEE.
- Yin, F., Lewis, P. E., Gomez-Dans, J., Wu, Q. (2019). A sensor-invariant atmospheric correction method: Application to Sentinel-2/MSI and Landsat 8/OLI. EarthArXiv 2019. **Preprint**.
- Yuan, D., & Elvidge, C. D. (1996). Comparison of relative radiometric normalization techniques. *ISPRS Journal of Photogrammetry and Remote Sensing*, 51(3), 117–126.

Publisher's Note Springer Nature remains neutral with regard to jurisdictional claims in published maps and institutional affiliations.

Springer Nature or its licensor holds exclusive rights to this article under a publishing agreement with the author(s) or other rightsholder(s); author self-archiving of the accepted manuscript version of this article is solely governed by the terms of such publishing agreement and applicable law.